Estimation of the probability density function of random displacements from images

Adib Ahmadzadegan ⬥, Arezoo M. Ardekani ⬥, and Pavlos P. Vlachos ⬥*

School of Mechanical Engineering, Purdue University, West Lafayette, Indiana 47907, USA

We introduce an image-based algorithm to find the probability density function (PDF) of particle displacements from a sequence of images. Conventionally methods based on cross correlation (CC) of image ensembles estimate the standard deviation of an assumed Gaussian PDF from the width of the CC peak. These methods are subject to limiting assumptions that the particle intensity profile and distribution of particle displacements are both Gaussian. Here, we introduce an approach to image-based probability estimation of displacement (iPED) without making any assumptions about the shape of particles' intensity profile or the PDF of the displacements. In addition, we provide a statistical convergence criterion for iPED to achieve an accurate estimate of the underlying PDF. We compare iPED's performance with the previous CC method for both Gaussian and non-Gaussian particle intensity profiles undergoing Gaussian or non-Gaussian processes. We validate iPED using synthetic images and show that it accurately resolves the PDF of particle displacements with no underlying assumptions. Finally, we demonstrate the application of iPED to real experimental data sets and evaluate its performance. In conclusion, this work presents a method for the estimation of the probability density function of random displacements from images. This method is generalized and independent of any assumptions about the underlying process and is applicable to any moving objects of any arbitrary shape.

I. INTRODUCTION

Evaluating the probability density function (PDF) of particle displacements has many applications, for example, measuring diffusion coefficient of particles in a liquid medium [1,2], microrheology [3], temperature measurements [4,5], quantifying Reynolds stresses in turbulent flows [6], and uncertainty quantification in velocity measurements [7].

There are mainly two approaches to find the PDF of displacement from images of moving particles, namely, tracking based and correlation based. The first technique is using particle tracking velocimetry (PTV) methods which involve individually tracking particles over time to find the PDF of displacements [8]. Despite the wide use of PTV methods for diffusion and rheology measurements, PTV methods face two major limitations. First, they are subject to particle detection and localization errors. Moreover, PTV methods cannot be used for high concentration particle suspensions or high feature-density images since they fail to find the correct trajectories when two or more particles cross each other's paths.

Unlike PTV, which focuses on the individual particles in the domain, particle image velocimetry (PIV) finds the cross correlation (CC) of consecutive particle image patterns without detecting individual particles. Therefore, PIV can work with low- and high-density image patterns and it is more computationally efficient compared to PTV given the convergence achieved. Note that PIV methods applied to systems with low particle concentrations need more images to converge compared to PTV methods.

In PIV, the most probable displacement of tracer particles is found from the location of the cross-correlation peak in space. It has been shown that the cross-correlation peak is the convolution of particle displacements and particle intensity profile [6]. Previous researchers have used this information to find the width of the cross-correlation peak and relate that to Reynolds shear stresses or Brownian motion of the particles within an image domain [1,2,4,5]. These studies model the PDF by making two assumptions, first that the particle intensity profile is Gaussian and second that the underlying PDF of displacement follows a Gaussian distribution. Therefore, the width of the PDF of displacement can be calculated using Eq. (1),

$$C_w = \sqrt{P_w + 2D_p^2},$$

(1)

where C_w is the width of the peak of ensemble CC, D_p is the particle diameter found from the spread of autocorrelation (AC), and P_w is the width of the PDF of displacements, where CC and AC are defined as shown in Eqs. (2) and (3) respectively,

$$C_{\text{cross}}(s) = \int I_1(X)I_2(X+s)dX,$$

(2)

$$C_{\text{auto}}(s) = \int I_1(X)I_1(X+s)dX,$$

(3)

where I_1 and I_2 represent the two images, X is the image coordinate, and s is the spatial shift between the two images [9]. It is important to note that only the width of the PDF can be found using Eq. (1) while the PDF of displacements and similarly CC and AC are two-dimensional (2D) matrices which are sometimes referred to as planes. This method of

*pvlachos@purdue.edu

033305-1

estimation of the width of the PDF from CC will be referred to as probability spread estimation from cross correlation (PSEC) in this paper. PSEC is reported to have an estimated accuracy of 8% when used for diffusion measurements under ideal conditions [4], and it is more computationally efficient compared to PTV. However, PSEC is strictly limited to systems with a Gaussian particle intensity profile (i.e., no out-of-focus effects, no arbitrary particle shapes) and a Gaussian PDF of displacements. In many practical applications, these assumptions do not hold and using PSEC can lead to a wrong estimation of the PDF, and as a result a wrong measurement of the properties of interest that are derived from the PDF, such as diffusion coefficient or temperature.

In this paper, we propose a generalized cross-correlation based method which directly finds the two-dimensional PDF of displacements by deconvolving the CC from the AC. This cross-correlation deconvolution belongs to a subcategory of the generalized cross-correlation (GCC) methods, called smoothed coherence transform (GCC-SCOT) [10]. In the process of finding the PDF of displacements using GCC-SCOT, we make no assumption on the particle intensity profile nor the nature of the process which dictates the underlying PDF of displacements. So, this algorithm can be directly applied to systems with arbitrarily shaped particles undergoing arbitrary PDF of displacements. Deconvolution in the spatial domain is mathematically complex and computationally expensive, however in the spectral domain the deconvolution is simplified to division. This deconvolution which is applied to the average of cross-correlation planes preserves the phase information of the spectral cross correlation which corresponds to the most probable displacements [11,12] and removes only the contribution of particle shape which is part of the magnitude of the spectral correlation planes [13]. We term this method Image-based probability estimation of displacements (iPED). In this paper, we use "particles" as a representation for all "moving features" in an image domain. However, the proposed method can be applied to any moving object of any arbitrary shape.

This paper is divided into four sections. Section II discusses the implementation of iPED, and we explore its convergence. This is followed by assessments of iPED's performance using synthetic images in Sec. III, where the accuracy of the algorithm is compared to PSEC. This section is divided into two main parts: Gaussian and non-Gaussian processes, where the PDF of the displacements follows Gaussian or non-Gaussian distributions. Each is then studied for particles with Gaussian and non-Gaussian intensity profiles. Finally, in Sec. IV, experimental data sets are used to evaluate iPED's performance for measurement of diffusion coefficient of known sized particles.

II. METHODOLOGY

A. Implementation of iPED

iPED is a cross-correlation based method to find the PDF of particle displacements, undergoing random motions within regions of interest (ROIs) of images. We summarize the algorithm in Fig. 1 and the flowchart for implementation of iPED is shown in Fig. 2. Images are the input of the iPED
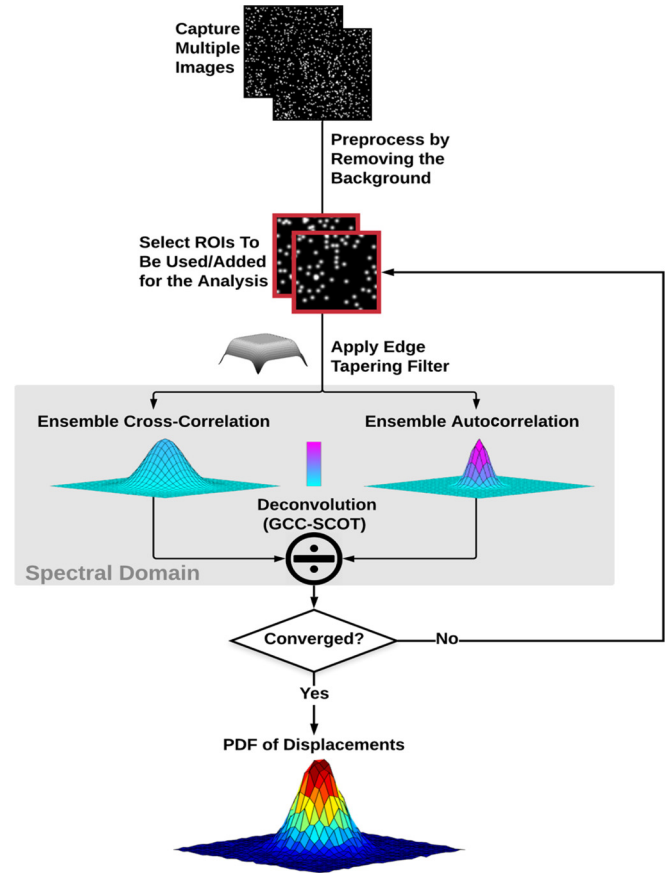
FIG. 1. iPED algorithm.

and the output is the PDF of the displacements as shown in Figs. 1 and 2. In order to get the PDF of displacements from the crosscorrelation, the contribution of particle shape, image noise, and background to the CC must be removed. This is to gain the information about the possible displacements within the two ROIs.

Image preprocessing is performed as the first step to remove the contribution of unwanted patterns to the PDF. We subtract the average image of the time series from all the individual images in order to remove the background intensity and static patterns from the images. Preprocessing is crucial if static patterns are present in the images, which can alter the PDF by contributing zero displacements to the distribution. The preprocessed images are then divided into ROIs with defined sizes and ROIs are used to calculate the cross correlations. The effects of the size of the ROIs on accuracy and rate of convergence are discussed later in the paper.

Spatial cross-correlation operation is simplified to a multiplication in Fourier domain. Multiplications are mathematically simpler and computationally more efficient. Therefore, conventionally in PIV processing, cross correlations and autocorrelations are evaluated in Fourier space. In order to perform the calculations in Fourier space, image ROIs are transformed from Cartesian (spatial) domain into Fourier (wave number) domain (shown as a grey box in Fig. 1). Equation (4) shows the spectral cross correlation ($G_{I_1I_2}$),

$$G_{I_1I_2}(f) = \mathcal{F}(I_1) \times [\mathcal{F}(I_2)]^*, \qquad (4)$$
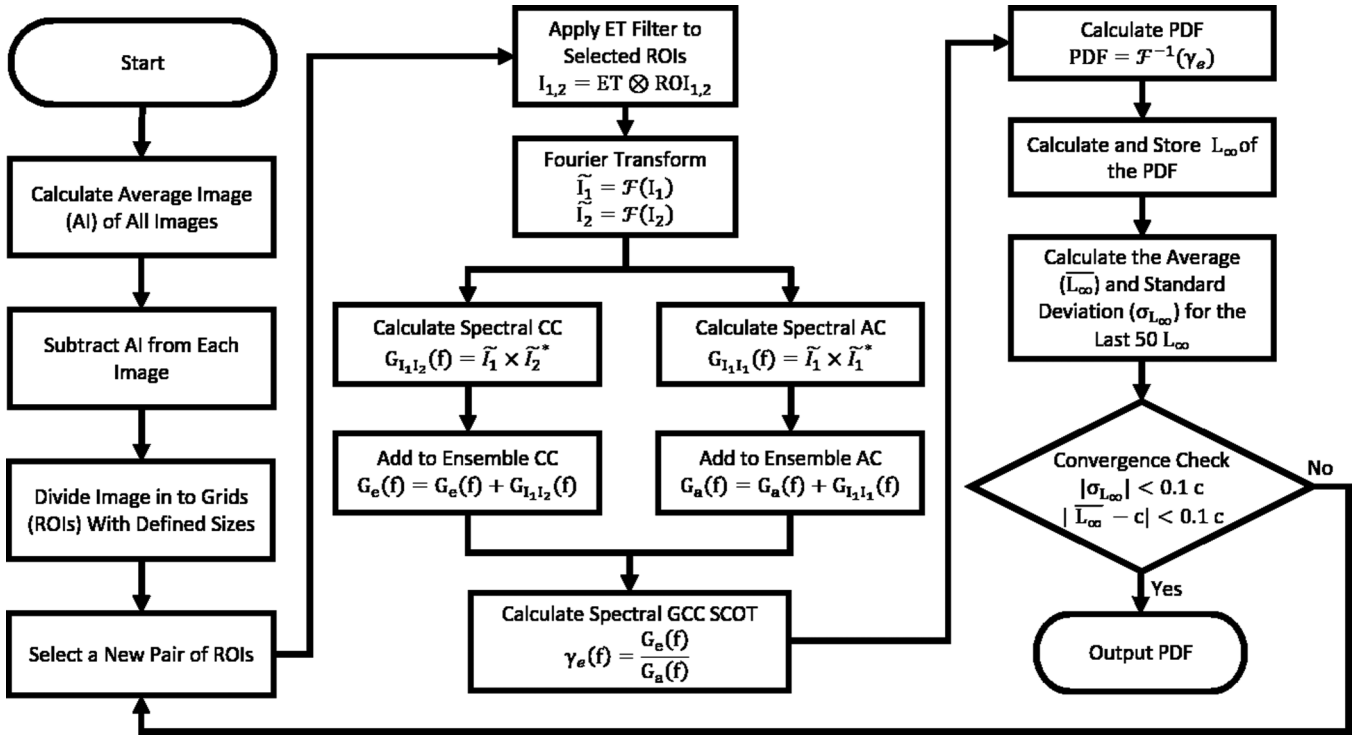
FIG. 2. Flowchart for iPED implementation.

where f is the spectral coordinate and I_1, I_2 represent image ROI 1 and ROI 2, respectively. $\mathcal{F}(I)$ is the Fourier transform of the ROI and * denotes the complex conjugate. The inverse Fourier transform of $G_{I_1 I_2}$ is the two-dimensional cross-correlation plane defined in Eq. (2) [10]. Spatiotemporal ensembles of CC and AC are individually calculated by adding the complex correlation planes of different ROIs in the spectral domain.

Conventionally in PIV processing, in order to reduce aliasing and edge effects in the frequency domain due to the nature of discrete Fourier transform, a Gaussian apodization window is applied to the images prior to the Fourier transform [14]. Gaussian apodization weights the intensity of the particles in a nonuniform manner depending on the spatial location of the particles with respect to the ROIs boundary. This causes the measurement to be biased towards the center of the ROI, which is useful for PIV measurements. However, for measuring the PDF of particle displacements, the contributions of all particles in the ROI to the correlations must be kept equal. Thus, in order to maintain an equal weight for all particles while suppressing the edge effect, we use Gaussian edge tapering (ET) windowing function. Such apodization function leaves the majority of the ROI intact while tapering the edges of the ROI. We set the standard deviation of the Gaussian function in the tapering filter to be 3 pixels (px) across the boundaries. The Gaussian ET window is convolved with preprocessed ROIs. Subsequently, the ROIs are Fourier transformed and the correlations are evaluated in the frequency domain (see second column in Fig. 2).

To achieve the goal of recovering the PDF of the displacements from the CC, we use the GCC-SCOT filter. GCC-SCOT is a deconvolution of the autocorrelation from the cross correlation, and is used in order to remove the contributions of particle shape from CC and acquire the PDF of displacements. GCC-SCOT ($\gamma_{I_1 I_2}$) in the Fourier domain is defined as the following [10]:

$$\gamma_{I_1 I_2}(f) = \frac{G_{I_1 I_2}(f)}{\sqrt{G_{I_1 I_1}(f) G_{I_2 I_2}(f)}}. \tag{5}$$

The autocorrelation used for the deconvolution is the geometric average of autocorrelation of ROI 1 and ROI 2. If the shape of the particles from ROI 1 to ROI 2 is the same, then Eq. (5) can be simplified such that only autocorrelation of the first image is used. The inverse Fourier transform of $\gamma_{I_1 I_2}$ is a plane that shows all the possible displacements of particles between the two frames. Instead of using the pairwise $\gamma_{I_1 I_2}$, we used the spatiotemporal ensemble of CC and AC in Eq. (5) as shown in the second column of Fig. 2. The reason for using the ensemble and details of the calculations of correlations are discussed in the next section.

After performing the deconvolution in the spectral domain, the result is transferred to the spatial domain (see the third column in Fig. 2). The resulting PDF is tested against the convergence criterion. If convergence is not achieved, more image ROIs will be added to the ensemble until the convergence criterion is met. The converged PDF of displacements is the output of iPED as shown in Fig. 1. Details of the convergence assessment is discussed later in this paper.

B. Theoretical foundations of image-based probability estimation of displacements

An image ROI of particle patterns can be described by $I(X)$, where I is the intensity field as a function of position (X). The
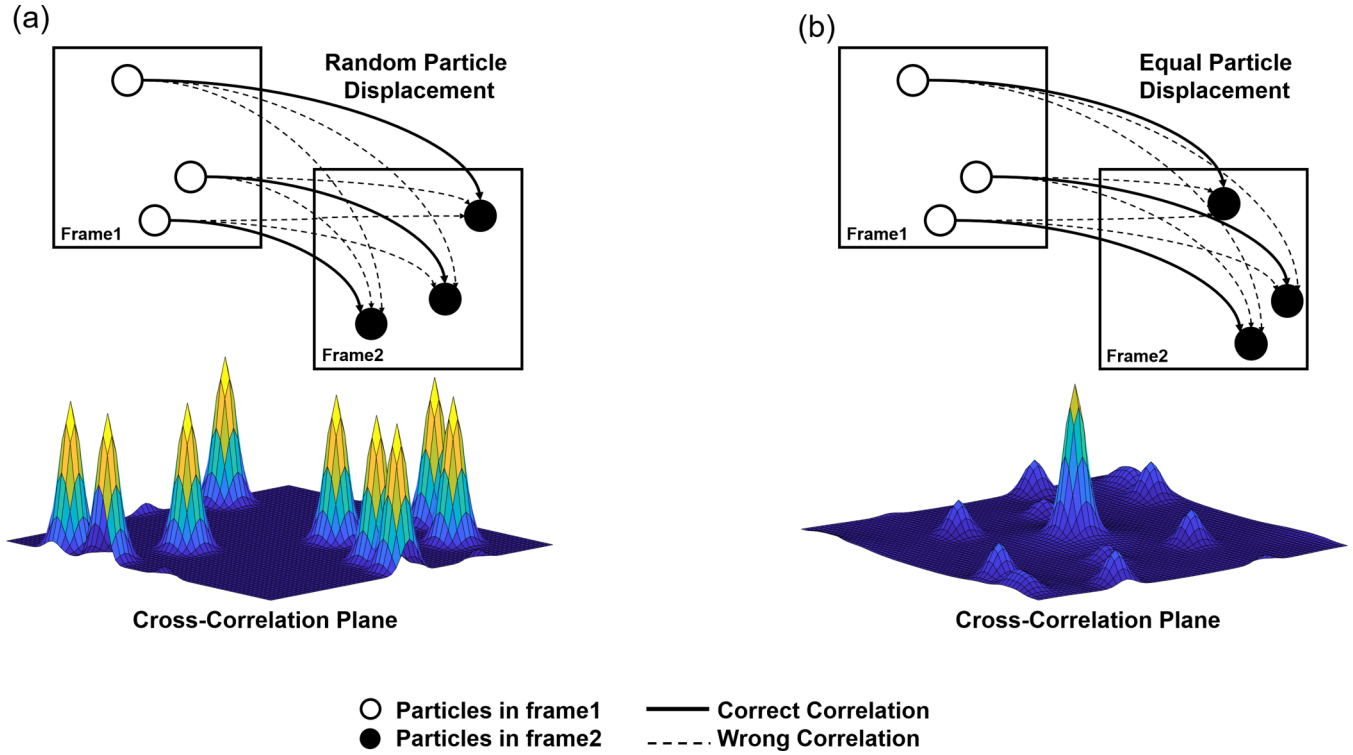
FIG. 3. Cross correlation of two ROIs, (a) with random particle displacement and (b) with equal particle displacement.

intensity field contains patterns from N_p number of particles with the same intensity profile, i.e., point spread functions (I_p). The locations of particles in space are represented as Dirac delta functions (δ) with peaks at the center of each particle (X_i):

$$I(X) = I_p \otimes \sum_{i=1}^{N_p} \delta(X - X_i). \tag{6}$$

Assuming there is no loss of correlation, i.e., all particles remain inside the two regions of interest (ROI) that are being correlated, the standard cross-correlation plane (in spatial domain) of the two ROIs can be described as in Eq. (7). We decompose cross correlation (C_{cross}) into the main signal (C_{signal}) and noise (C_{noise}). The relative displacement of particle "i" from the first ROI to particle "j" from the second ROI is represented as $d_{i,j}$,

$$C_{\text{cross}}(X) = A \otimes \sum_{i=1}^{N_p} \delta(X - d_{i,i})$$
$$+ A \otimes \sum_{i=1}^{N_p} \sum_{j=1}^{N_p} (1 - \delta_{i,j}) \delta(X - d_{i,j})$$
$$= C_{\text{signal}}(X) + C_{\text{noise}}(X), \tag{7}$$

where $\delta_{i,j}$ is 1 when $i = j$ and 0 otherwise. As shown in Eq. (7), each particle-particle convolution results in a "unit" peak in the correlation plane with the shape of $A = I_p \otimes I_p$ located at the relative distance of particles i and j within the two frames. There is a total of N_p^2 particle-particle convolutions in the CC plane. As an example, we show a pair of ROI

in which there are three particles and each move randomly in the domain in Fig. 3(a) and the corresponding CC shows $3^2 = 9$ unit peaks that show all the possible particle-particle correlations within the two frames. Among all the N_p^2 unit peaks, N_P of them correspond to the "correct matches" of particles between the two frames. The correct match is when a particle in image 1 is convolved with itself in image 2. Correct matches are represented in the first sum in Eq. (7) and we refer to them as the signal portion of the cross correlation (C_{signal}). Finding the correct N_P peaks requires further information as in the case of random displacements; it is almost impossible to distinguish the correct peaks among the N_P^2 number of total peaks. Finding the correct peaks in the case of ideal PIV images, where all (most) of the particles follow the same displacement, is rather straightforward as all the correct particle-particle correlations are positioned in the same location of the CC plane causing the most probable displacement to stand out compared to all the other wrong correlations [shown in Fig. 3(b)].

In the CC plane, there are $N_P^2 - N_P$ number of wrong matches between particles that contribute to C_{noise}. Uncorrelated background noise and differences in average image intensities contribute to the noise as well [9]. In order to find the PDF of the displacement within the ROI, identifying the contribution of correct particle matches from the contribution of the wrong matches is crucial.

Meinhart et al. [2] showed that if the flow field is steady or quasisteady, the contribution of C_{noise} to CC compared to C_{signal} can be significantly diminished by taking the average of multiple CC planes found from correlation of each consecutive image pair [2]. If the number of correlations ensembled is N, the contribution of noise is scaled by $1/\sqrt{N}$.

Ensemble correlations can be performed in space by taking the average CC of different ROIs within a pair of images or it can be implemented in a temporal sense, where the CC planes of sequential pairs of ROIs are averaged in time. Spatial or temporal ensembles both can suppress the effect of C_{noise}, however, if the spatial variation of the PDF is under investigation then the temporal ensemble for ROIs is to be used to achieve a spatially resolved PDF. In situations, where there is not enough temporal information, the spatial ensemble is more applicable to achieve a converged measurement of the PDF of displacements. In this work, since the PDF is spatially and temporally invariant, we performed the spatiotemporal ensemble.

We performed the spatiotemporal ensemble in the spectral domain by averaging the complex correlation planes (grey box in Fig. 1) to improve the computational efficiency. By implementing the ensemble approach, we suppress the contribution of C_{noise} to CC such that CC can be approximated by C_{signal}. As mentioned earlier, C_{signal} is the convolution of PDF of displacements with the average autocorrelation (AC) of the particle intensity profile.

In the AC plane, a frame is correlated with itself so there is no displacement involved and the PDF of displacements is a Dirac function at zero. So, the shape of the AC solely represents the average particle intensity distribution. We find the average AC of ROIs by performing the ensemble autocorrelation of images. Ensemble AC ensures that AC is converged to include only the correct particle-particle matches.

We then relate the cross correlation (C_{cross}) to the PDF of displacements (P_D), and autocorrelation (C_{auto}) using Eq. (8). This step is performed in the Fourier space using the GCC-SCOT filter as shown in Eq. (9).

$$C_{\text{cross}} = C_{\text{auto}} \otimes P_D, \tag{8}$$

$$P_D = \mathcal{F}^{-1}\left(\frac{\mathcal{F}(C_{\text{cross}})}{\mathcal{F}(C_{\text{auto}})}\right), \tag{9}$$

where $\mathcal{F}$ and $\mathcal{F}^{-1}$ show the Fourier transform and inverse Fourier transform, respectively. The resulting PDF is a bivariate probability density function of displacements such that its integral is equal to unity. Since this PDF is found using an ensemble approach, the greater the number of ROIs that are used, the more accurate measurement of PDF is achieved. In the next section, we introduce a convergence test for iPED measurements to stop the algorithm from performing more ensembles when the PDF convergence is ensured.

C. Convergence criterion

For a converged evaluation of the PDF using iPED there are two important factors to consider. First is that the total number of contributing displacements ($N \times N_p$) must be large enough to represent the underlying PDF of displacements. If the shape of the PDF of displacement is simple such as a Dirac or a normal distribution, the required number of observations (displacements) for a reliable estimation of the PDF is lower compared to a more complex PDF such as a multimodal. The second important factor is that a high signal-to-noise ratio (SNR) in the correlation plane must be achieved.

We ensure a high SNR by monitoring the change in L_∞ of the estimated PDF as a function of ensemble number. L_∞ can be fitted to $L_\infty = \frac{a}{\sqrt{N}} + c$, where a and c are the fitting parameters, noting that c represents the value of the L_∞ with an infinite number of images. The convergence is defined to be achieved when the average L_∞ of the last 50 added image ensembles is within 10% from the "c" found for the last image ensemble and the standard deviation of L_∞ of the last 50 image ensembles is within 10% of the mean value.

There are two factors that affect the rate of convergence of iPED. The first one is the size of the ROI and the second is the amount of background noise present in images. In the next sections, we study the effects of dividing images into smaller ROIs on the rate of convergence using synthetic images. In the noise analysis section, we show that a higher noise level will delay the convergence of iPED.

D. Synthetic image generation

We synthetically generated 8-bit images of particles undergoing random displacements. The simulation domain was five times bigger than the chosen image size and particles with a concentration of 0.005 particles per squared pixels (px) were placed in random locations in space. We generated 10 000 8-bit images whose dimensions were $256 \times 256 \, \text{px}^2$. In the section that the size of the interrogation regions is studied the window size is chosen to be $2048 \times 2048 \, \text{px}^2$. To account for the imaging noise, 10% uncorrelated zero-mean Gaussian noise was added to each pixel in each image. In the noise analysis section, the noise level within the images was varied from 0% to 75%. Particle displacements within frames were randomly drawn from an input probability density function.

We consider particles with Gaussian-shaped intensity profile in one case and non-Gaussian shaped in another case. Gaussian particle intensity profiles are generated using a Gaussian function such that the diameter of particles are varied from 3 to 10 pixels for the particle size study section and is chosen to be 5 pixels for all the rest of the cases [see Fig. 4(b)] [15]. For the case of non-Gaussian particle intensity profiles, the absolute value of a Bessel type I intensity profile was simulated such that the central region of particles has the same size as the Gaussian particle intensity profiles (5 px) and the fringe pattern (rings) extend to 10 px for each particle [see Fig. 4(c)]. This choice of particle intensity profile is such that the generated particle images are qualitatively similar to what is observed in images of perfectly focused spherical particles (Airy function) or particle images with spherical aberrations commonly observed in lenses with high numerical aperture [16]. Similar patterns are also present in holography images [17] and Bessel beam microscopy systems [18].

E. Methodology for error analysis and validation

PSEC is developed to work with systems for which the displacement PDF follows a Gaussian distribution. Such a PDF describes Brownian diffusion of spherical particles in Newtonian fluids. In a 2D image plane, the Gaussian PDF of

displacements is represented as in Eq. (10)

$$\text{PDF}(\Delta x, \Delta y, t) = A \times \exp\left(-\frac{(\Delta x - \overline{\Delta x})^2}{2\sigma_x^2} - \frac{(\Delta y - \overline{\Delta y})^2}{2\sigma_y^2}\right),$$

(10)

where A is the peak height, $\overline{\Delta x}$, $\overline{\Delta y}$ are the peak location, and σ is the standard deviation of the Gaussian profile. The standard deviation $\sigma = \sqrt{2Dt}$, where D is the diffusion coefficient and t is the time lag. In the case where the PDF of the displacement follows a Gaussian distribution, we fit Eq. (10) using a least square fit [19] to all the points of the PDF function and find D.

To compare iPEDs performance to PSEC, PSEC is implemented based on Chamarthy *et al.* (2009) while no apodization window is used and ensembles are performed in the real space [5]. The width of CC and AC are measured as 4σ, where σ is found from a least square fit of a 2D Gaussian function to correlation planes. PSEC and iPED are both performed with an interrogation region (IR) size of $64 \times 64 \, \text{px}^2$. The iPED method is performed as mentioned in Secs. II A and II B. Since there are no convergence criteria for the model-based PSEC method when it comes to resolving the PDF of the displacements, we report all the results at the ensemble count corresponding to when iPED is converged. We compare the measured PDF from both methods with the expected PDF. For those cases where the input PDF is a Gaussian function, the resulting diffusion coefficient values are used for comparison and error analysis.

F. Size of interrogation regions

Next, we study the effect of interrogation region (IR) size on the rate of convergence. Dividing images into smaller IRs provides a greater number of spatial ensembles in the correlations resulting in a better SNR (since the contribution of noise with N ensemble is scaled by $1/\sqrt{N}$) which results in convergence with a smaller number of full images, i.e., more ROIs are achieved from less images using the spatial ensemble.

Another effect of smaller IRs is that the noise in the correlations is suppressed due to a lower number of particles present in the smaller ROIs. Let us assume that the total number of particles in an image series is N_p. Dividing the image into M^2 number of IRs results in $N_{\text{IR}} = \frac{N_p}{M^2}$ number of particles in each IR. Therefore, the number of wrong particle correlations for each IR is $N_{\text{IR}}^2 - N_{\text{IR}}$ and the total number of the correct correlation peaks is N_{IR}. If we add all the M^2 individual IR correlations, then the total number of correct particle

correlations is $M^2 \times N_{\text{IR}}$ which is equal to N_p, the number of correct peaks if full sized image correlations were used. This means that the number of correct particle correlations remains the same independent of the size of the IR. However, if we add all the numbers of wrong particle correlations in all IRs, the total number is $M^2 \times (N_{\text{IR}}^2 - N_{\text{IR}}) = \frac{N_p^2}{M^2} - N_p$. Note that full image correlations as discussed previously leads to $N_p^2 - N_p$ wrong correlations. This means that the number of wrong correlations contributing to the noise in the correlation plane is suppressed by a factor of M^2 if the image is divided into M^2 smaller IRs and therefore a faster convergence is achieved due to the SNR improvement.

We test the effect of IR size on the convergence using synthetically generated images of particles with Gaussian intensity profiles undergoing a Gaussian PDF of displacement (with diffusion coefficient of $5\frac{\text{px}^2}{\text{Frame}}$), where the size of images is $2048 \times 2048 \, \text{px}^2$ with 10% noise level. We processed ten independent cases of such images with different IR sizes. We show that the total number of images required for convergence of iPED is much lower if smaller IR sizes (and as a result, a greater number of IR windows) are used. For example, with a 64×64 IR size, iPED converges with a total of seven full sized images with 3.96% error in the measurement of diffusion coefficient while for a 256×256 IR size 53 full images are required to achieve an error of 0.46%. In Table I, we summarize the required average number of images and IRs for different IR sizes. We also report the error in the diffusion measurement and standard deviation of the error for ten replicates using both iPED and PSEC for each IR size. The reason that larger IR sizes show a lower error value is that larger and less noisy 2D fields of PDF are acquired for those cases and the least square Gaussian fit finds a better estimation of the diffusion value.

Although smaller IR size promotes a faster convergence, the IR size must be chosen large enough such that the majority of the particles in one IR remain in the same IR in the next frame that it is being correlated to. This is why the measurement's accuracy is improved with larger IR sizes in Table I. Therefore, similar to PIV processing, we suggest that the minimum IR is four times bigger than the estimated displacement of the particles within the frames such that at least half of the particle population has a corresponding match between the frames. The convergence can be further improved with a window shifting technique if the mean displacement within the ROI is nonzero and the amount of random displacement is within 0.5 pixels. Window shifting should be implemented such that there is no window overlap as that

TABLE I. Effect of IR size on convergence.

IR size	32×32	64×64	128×128	256×256	512×512	1024×1024
Average number of images used to achieve convergence	2	7	15	53	187	718
Avergae number of IRs used to achieve convergence	3941	6068	3878	3350	2997	2873
% error in measurement iPED	14.25 ± 1.80	3.96 ± 1.09	1.61 ± 0.56	0.46 ± 0.25	0.12 ± 0.08	0.26 ± 0.06
% error in measurement PSEC	37.38 ± 1.18	15.62 ± 0.79	6.17 ± 0.77	2.22 ± 0.39	0.49 ± 0.32	0.31 ± 0.20
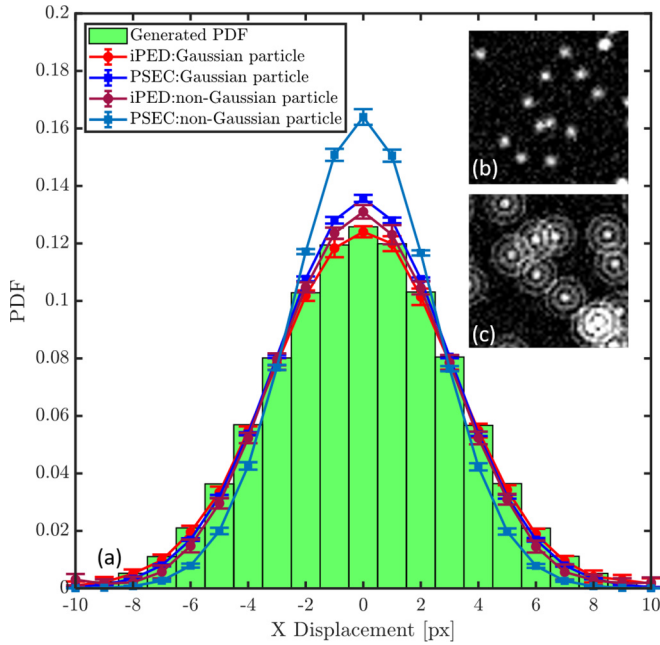
FIG. 4. (a) Comparison of the generated Gaussian PDF to iPED and PSEC. Image of particles with (b) Gaussian (c) non-Gaussian intensity profiles.

can cause some particles to contribute more than once to the measured PDF.

III. RESULTS AND DISCUSSION: PERFORMANCE ASSESSMENTS OF iPED USING SYNTHETIC IMAGES

In this section, we evaluate the performance of iPED and compare it to PSEC using synthetic images. We divide these analyses in two main categories, namely, Gaussian processes and non-Gaussian processes. Each category consists of the study of Gaussian and non-Gaussian particle intensity profiles. For the case of non-Gaussian processes, we provide several examples to cover a wider range of applications.

A. Gaussian processes

The Gaussian process that we study in this paper is the diffusion of spherical particles. Diffusion is modeled as random displacements drawn from a 2D Gaussian distribution with a zero mean and a standard deviation of $\sigma = \sqrt{2D\tau}$, where D is the Stokes-Einstein diffusion coefficient [20] which is set to be 5 $[\frac{\mathrm{px}^2}{\mathrm{Frame}}]$ and τ is the time lag between images which is set to be 1 frame. We generated 20 independent synthetic image sets to compare the iPED estimation of the diffusion coefficient to that of PSEC.

The green bar chart in Fig. 4(a) shows the generated PDF of the displacements for the particles with Gaussian

and non-Gaussian intensity profiles. The estimated PDF of displacements in the X direction $[\int_{-\infty}^{\infty} \mathrm{PDF}(x, y) dy]$ found from both iPED and PSEC are shown in Fig. 4(a). Error bars show the standard deviation of 20 independently generated images from the same prescribed PDF. The resulting diffusion coefficient for the particles with Gaussian intensity profiles [shown in Fig. 4(b)] using iPED shows $3.75 \pm 1.01\%$ error while the PSECs estimation has $13.52 \pm 1.58\%$ error. The estimated D for particles with non-Gaussian intensity profiles [shown in Fig. 4(c)] with iPED has $9.61 \pm 0.67\%$ error while the PSECs estimation shows $40 \pm 1.98\%$ error. So iPED provides approximately four times better measure of the diffusion coefficient value in both cases. Note that violation of the underlying assumptions of PSEC causes a deteriorated estimation of the PDF which is manifested in all the cases in this section, except the diffusion of particles with Gaussian intensity profiles. Therefore, PSEC shows its best performance on estimating the generated PDF and consequently the diffusion coefficient for the particles with Gaussian intensity profiles in Fig. 4(a), because its underlying assumptions are met.

1. Noise analysis

Experimental images are often associated with some level of thermal noise due to the sensitivity of the imaging devices. In this section, we study the effect of noise on the performance of iPED and compare it against PSEC using synthetic images. To mimic imaging noise in real systems, we added uncorrelated Gaussian noise to each pixel, with a mean value of 0 and a standard deviation that is defined as a percentage of pixel peak intensity.

We use synthetic images where Gaussian particles undergo a Gaussian process ($D = 5$ $[\frac{\mathrm{px}^2}{\mathrm{Frame}}]$), in order to quantitatively compare iPED's measurement of the diffusion coefficient to that of PSEC while changing the noise level in the images. We generated 20 independent data sets for noise levels of 0%, 25%, 50%, and 75%.

We present the error in diffusion coefficient measurements of both methods for different noise levels in Table II. We show that iPED consistently provides lower bias error in the diffusion measurement by a factor of about 2 and a lower random error by a factor of approximately 3. We also show that the number of images required for convergence increases as the noise level increases (see Table II). We plot the measured diffusion coefficients normalized by the expected value in Fig. 5. The box plots show the median and one quartile above and below the median as well as the minimum and maximum measurements. Inset images in Fig. 5 show representative examples of the images with different noise levels. The results confirm that iPED consistently provides a better estimate of the diffusion coefficient compared to PSEC.

TABLE II. Noise effects on the accuracy and convergence.

Noise level	0%	25%	50%	75%
% error in iPED measurement	4.58 ± 0.82	1.81 ± 0.86	6.12 ± 0.87	13.00 ± 1.03
% error in PSEC measurement	8.11 ± 2.64	5.02 ± 2.54	17.86 ± 2.47	19.01 ± 2.45
Average number of full images required for convergence	481	397	832	2322
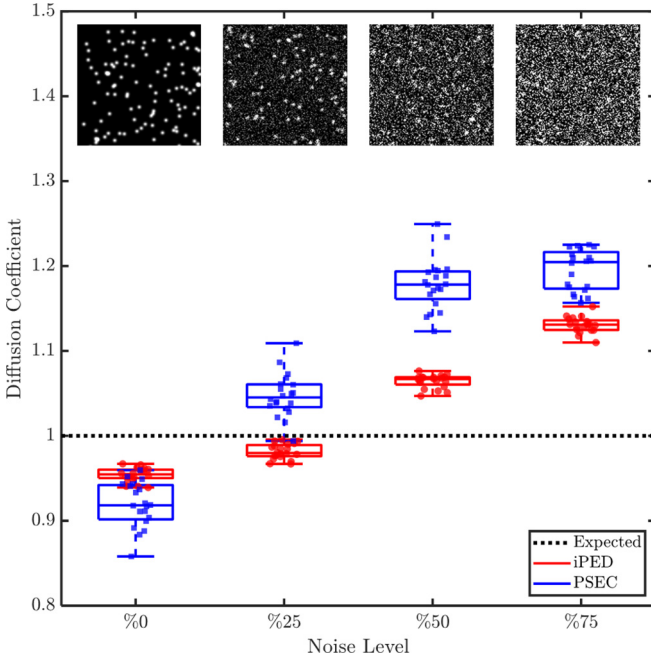
FIG. 5. Normalized diffusion coefficient vs image noise levels are shown as box plots. The blue square markers represent PSEC results and red circle markers show iPED results. One representative image of each noise level is shown. The expected normalized diffusion value is 1.

2. Particle size analysis

The size of the particles in the images are shown to affect the accuracy of PIV measurements [21]. We studied the effect of the particles' size by varying the diameter of particles with Gaussian intensity profiles from 3 to 10 px. We generated
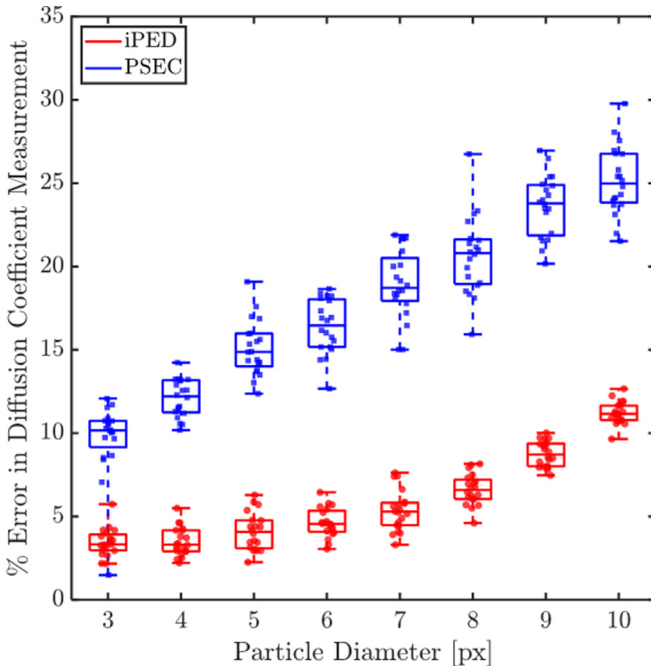
FIG. 6. Error in the diffusion measurement vs particles diameter. The blue square markers represent PSEC results and red circle markers show iPED results.

synthetic images with Gaussian PDF of displacement ($D = 5$ [$\frac{\mathrm{px}^2}{\mathrm{Frame}}$]) and studied 20 independent cases for each particle size.

We report the error in the diffusion coefficient measurement using both iPED and PSEC for different particle sizes in Fig. 6, where the box plots show the median and the quartiles of the 20 runs. We show that the accuracy of iPED is consistently higher than the PSEC for all the particle sizes. The measurement error for iPED where the particle size is 5 px is shown to be approximately 4% while PSEC shows approximately 15% error in the diffusion measurement. Figure 6 shows that for particle sizes from 3 to 6 px the accuracy of iPED is not affected by the size of the particles however PSEC seems to work best with smaller particles.

B. Non-Gaussian processes

1. Zero mean Laplace distribution

Non-Gaussian PDFs are observed in several systems, for example in particle transport through porous media [22–26], tracers motions in colloidal suspensions, or in the presence of active swimmers [27–31]. Laplace PDF of displacement has been broadly used to model some of the non-Gaussian processes such as diffusive diffusivity [30,31]. Here, we generated particles with Gaussian and non-Gaussian intensity profiles similar to case of the Gaussian process, but in this case, the displacements are randomly drawn from a zero mean Laplace distribution shown in Eq. (11),

$$f(\Delta x, \Delta y | b) = \frac{1}{2b}\left[\exp\left(-\frac{|\Delta x|}{b} - \frac{|\Delta y|}{b}\right)\right], \qquad (11)$$

where Δx, Δy are the displacements in the Cartesian x, y directions and b defines the sharpness of the Laplace distribution.

We generated 20 independent cases for two cases of Laplace PDFs with standard deviations of 3.16 and 6 and both Gaussian and non-Gaussian intensity profiles were studied in this section.

We provide a comparison of the generated and estimated PDF of displacements in the X direction from both methods in Fig. 7. The green bar charts show the generated PDFs and the error bars show the standard deviation of 20 independent runs for iPED and PSEC. Figure 7 shows that using PSEC can lead to a wrong estimation of the PDF depending on how much different the underlying PDF is from a Gaussian profile, therefore iPED outperforms PSEC in this case and PSEC measurement deviates from the true PDF especially for higher b values.

2. Uniform distribution

Uniform distribution is a common PDF of displacement in a shear flow with homogeneous particle seeding. Particles with Gaussian and non-Gaussian intensity profiles are used similar to the previous cases and the displacements are randomly drawn from a uniform distribution shown in Fig. 8(b). We show a comparison of the generated and estimated PDF of displacements in the X direction at $y = 0$ using both iPED and PSEC for 20 independent cases in Fig. 8(a). The green bar chart shows the generated PDF and the error bars show
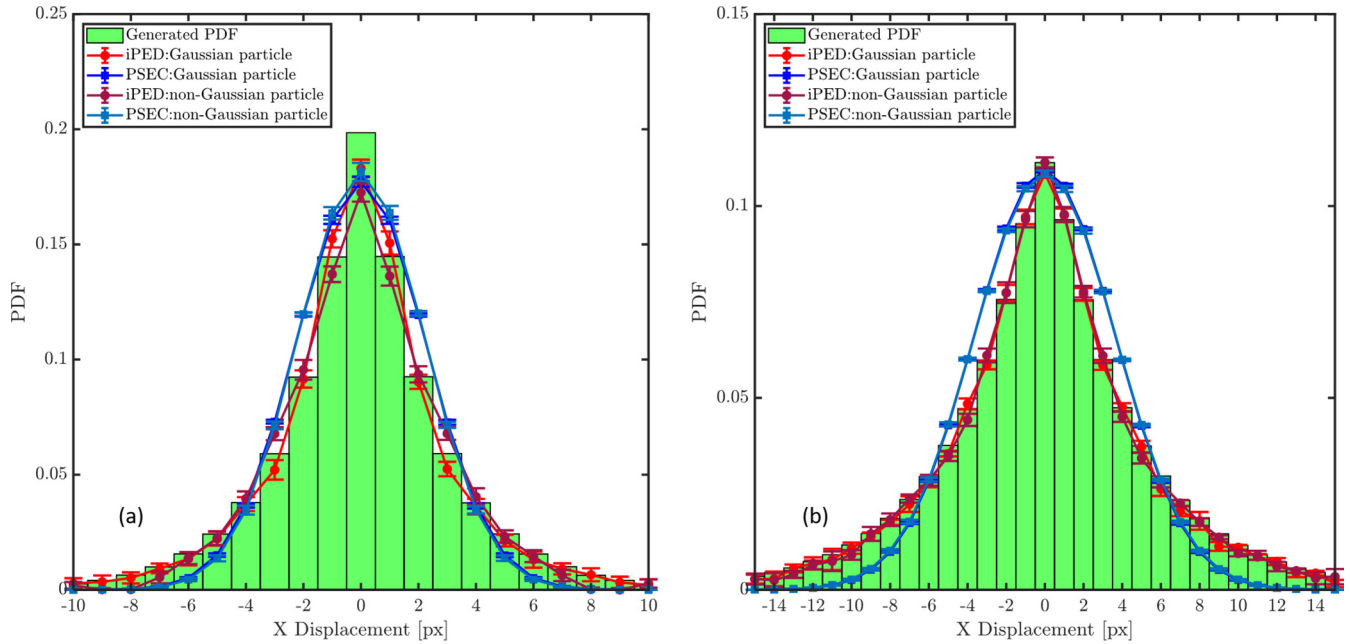
FIG. 7. Comparison of the generated PDF of the Laplace process to iPED and PSEC (a) where standard deviation of the PDF is 3.16, (b) where standard deviation of the PDF is 6.

the standard deviation of 20 independent runs for iPED and PSEC. Figure 8(a) shows that iPED provides a better estimation of the displacement PDF compared to that of PSEC.

This example shows that if the shape of the PDF does not have a rather sharp peak (unlike previous cases), iPED can still resolve the true shape of the PDF. The resulting PDF found from iPED can be used not only to find the standard deviation around the peak but also to provide more insight about the physics of the problem under investigation. For example, the

FIG. 8. (a) Comparison of the generated PDF to iPED and PSEC. (b) 2D generated uniform PDF of displacement.

PDF in this case can be used to report the minimum and maximum velocities captured in the field.

3. Multimodal PDF of displacements

The goal of generating a multimodal PDF is to show the power of iPED in resolving complex PDFs within the image domain. Here, Gaussian particles are generated, and the displacements are randomly drawn from a 2D displacement PDF shown in Fig. 9, where four Gaussian profiles with different standard deviations are superposed in different locations in space.

The generated and estimated PDFs of displacements in two dimensions using both methods are shown in Fig. 9. It shows qualitatively that iPED provides a more realistic estimate of the PDF compared to that of PSEC.

Since the PDF is more complex in this case compared to previous cases, the number of required images for convergence was higher than the previous cases (approximately 1000 vs 400 images). As expected, this suggests that if the underlying PDF of displacements within the images is complex, a greater number of images are required for a reliable estimation of the PDF.

IV. APPLICATION OF IPED ON EXPERIMENTAL DATA: DIFFUSION OF PARTICLES IN WATER

Analysis of particles' Brownian motion in a liquid medium is widely used in the literature to measure the diffusion coefficient, particle size, or microrheological properties of the liquid. This displacement of monodisperse particles in a Newtonian fluid is known to have a Gaussian PDF for displacements [20]. This Gaussian PDF as discussed in previous sections is related to the diffusion coefficient. We used
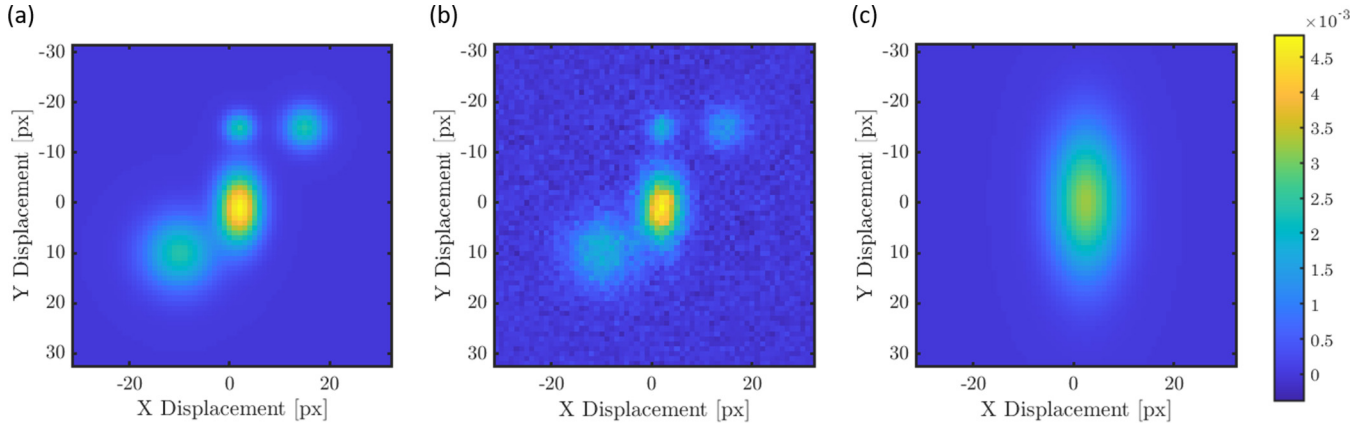
FIG. 9. (a) Two-dimensional generated PDF of displacement. (b) Estimated PDF from iPED. (c) Estimated PDF from PSEC.

this information to measure the diffusion value of known size particles.

Here, we captured experimental images of fluorescent polystyrene particles (Bangs Laboratories, Inc.) with known diameters, freely diffusing in water at room temperature. We diluted particles in water to a final concentration of 0.005% solids and added the sample between two cover glasses that are separated with a 500-μm spacer . We used a Nikon Ti-E microscope with an oil immersion 60$\times$ objective lens to capture 1000 12-bit 1024 $\times$ 1024 px^2 images at a rate of ten frames per second using a Phantom high-speed camera (model 630085), with a final pixel size of 0.16 μm.

We provide the iPED and PSEC's measurements of diffusion coefficient and the ground truth values which is calculated from the Stokes-Einstein equation [20] for different particle sizes in Fig. 10. The error bars show the standard deviation of 16 independent realizations for each particle size. Black error bars show the expected standard deviation in the
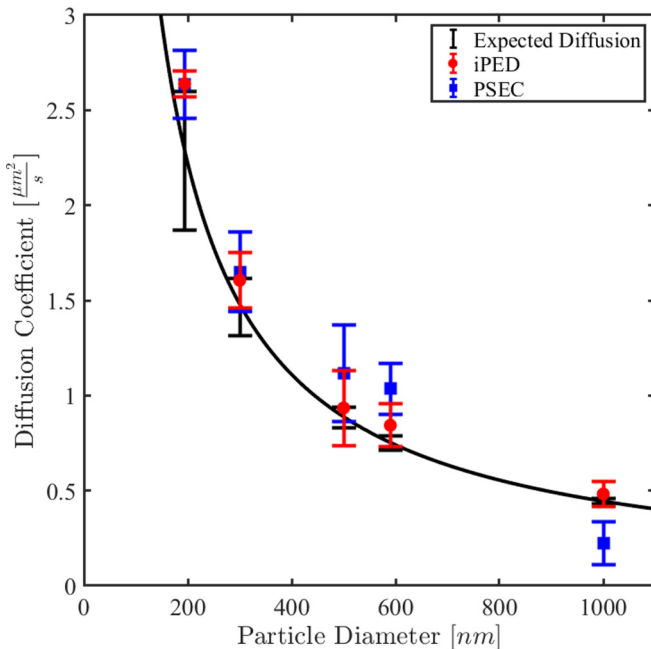
true diffusion due to the size distribution of particles reported by the manufacturer. We show that iPED provides a lower random error and lower bias error among all the particle sizes, for example, for 1-μm sized particles, PSEC shows approximately 50% error while iPED measurement overlaps with the expected diffusion coefficient value. The potential reason why PSEC is underperforming in these experiments is that the real experimental microscopy images of particles rarely have a perfect Gaussian-shaped intensity profile due to out-of-focus effects and the PSEC assumption for Gaussian particle intensity profile is not fully satisfied.

V. CONCLUSIONS

We developed and presented a generalized cross-correlation based method, to estimate the PDF of displacements from images of moving patterns, that requires no assumptions about the process PDF and the particles' intensity profile. We compared the results of iPED with the existing cross-correlation based method (PSEC) and showed approximately three times better accuracy in the measurements of diffusion coefficient using synthetic images. We also demonstrated iPED's performance on real experimental images for measuring the diffusion coefficient. Both experimental and synthetic images provide compelling evidence that the iPED method measures the PDF in a more robust and accurate way compared to the existing method.

We showed that iPED can reliably measure the PDF of displacements of objects within images. In this paper we used the resulting PDF to measure diffusion coefficient of particles as an example of the applications of PDF estimation. The PDF of displacements can also be used to find the Reynolds stresses or to report statistics of the flow field which is needed for example in uncertainty quantification [7].

Data are publicly available through the Purdue University Research Repository (PURR) [32]. A reference implementation of iPED can be found as an open-source code [33].

FIG. 10. Experimental diffusion coefficient measurement for different particle sizes.

[1] J. G. Santiago, S. T. Wereley, C. D. Meinhart, D. J. Beebe, and R. J. Adrian, A particle image velocimetry system for microfluidics, Exp. Fluids **25**, 316 (1998).

[2] C. D. Meinhart, S. T. Wereley, and J. G. Santiago, A piv algorithm for estimating time-averaged velocity fields, J. Fluids Eng. **122**, 285 (2000).

[3] P. Cicuta and A. M. Donald, Microrheology: a review of the method and applications, Soft Matter **3**, 1449 (2007).

[4] V. Hohreiter, S. T. Wereley, M. G. Olsen, and J. N. Chung, Cross-correlation analysis for temperature measurement, Meas. Sci. Technol. **13**, 1072 (2002).

[5] P. Chamarthy, S. V. Garimella, and S. T. Wereley, Non-intrusive temperature measurement using microscale visualization techniques, Exp. Fluids **47**, 159 (2009).

[6] S. Scharnowski, R. Hain, and C. J. Kahler, Reynolds stress estimation up to single-pixel resolution using PIV-measurements, Exp. Fluids **52**, 985 (2012).

[7] S. Bhattacharya, J. J. Charonko, and P. P. Vlachos, Particle image velocimetry (PIV) uncertainty quantification using moment of correlation (MC) plane, Meas. Sci. Technol. **29**, 115301 (2018).

[8] D. Ernst and J. Kohler, Measuring a diffusion coefficient by single-particle tracking: statistical analysis of experimental mean squared displacement curves, Phys. Chem. Chem. Phys. **15**, 845 (2013).

[9] R. D. Keane and R. J. Adrian, Theory of cross-correlation analysis of piv images,, Appl. Sci. Res. **49**, 191 (1992).

[10] C. Knapp and G. Carter, The generalized correlation method for estimation of time delay, IEEE Trans. Acoust., Speech, Signal Process. **24**, 320 (1976).

[11] A. C. Eckstein, J. Charonko, and P. Vlachos, Phase correlation processing for DPIV measurements, Exp. Fluids **45**, 485 (2008).

[12] A. Eckstein and P. P. Vlachos, Digital particle image velocimetry (DPIV) robust phase correlation, Meas. Sci. Technol. **20**, 055401 (2009).

[13] M. N. Giarra, J. J. Charonko, and P. P. Vlachos, Measurement of fluid rotation, dilation, and displacement in particle image velocimetry using a FourierMellin cross-correlation, Meas. Sci. Technol. **26**, 035301 (2015).

[14] A. Eckstein and P. P. Vlachos, Assessment of advanced windowing techniques for digital particle image velocimetry (DPIV), Meas. Sci. Technol. **20**, 075402 (2009).

[15] M. R. Brady, S. G. Raben, and P. P. Vlachos, Methods for digital particle image sizing (DPIS): comparisons and improvements, Flow Meas. Instrum. **20**, 207 (2009).

[16] M. Born and E. Wolf, *Principles of Optics* (Cambridge University Press, New York, 1999), p. 704.

[17] J. Katz and J. Sheng, Applications of holography in fluid mechanics and particle dynamics, Annu. Rev. Fluid Mech. **42**, 531 (2010).

[18] C. Snoeyink and S. Wereley, Single-image far-field subdiffraction limit imaging with axicon, Opt. Lett. **38**, 625 (2013).

[19] C. Tropea and A. L. Yarin, *Springer Handbook of Experimental Fluid Mechanics* (Springer Science & Business Media, New York, 2007).

[20] A. Einstein, The motion of elements suspended in static liquids as claimed in the molecular kinetic theory of heat, Ann. Phys. **322**, 549 (1905).

[21] M. Raffel, C. E. Willert, F. Scarano, C. J. Kähler, S. T. Wereley, and J. Kompenhans, *Particle Image Velocimetry: A Practical Guide* (Springer, New York, 2018).

[22] B. Wang, J. Kuo, S. C. Bae, and S. Granick, When Brownian diffusion is not Gaussian, Nat. Mater. **11**, 481 (2012).

[23] C. Xue, X. Zheng, K. Chen, Y. Tian, and G. Hu, Probing non-Gaussianity in confined diffusion of nanoparticles, J. Phys. Chem. Lett. **7**, 514 (2016).

[24] B. Wang, S. M. Anthony, S. C. Bae, and S. Granick, Anomalous yet brownian, Proc. Natl. Acad. Sci. USA **106**, 15160 (2009).

[25] S. Havlin and D. Ben-Avraham, Diffusion in disordered media, Adv. Phys. **36**, 695 (1987).

[26] A. V. Weigel, S. Ragi, M. L. Reid, E. K. P. Chong, M. M. Tamkun, and D. Krapf, Obstructed diffusion propagator analysis for single-particle tracking, Phys. Rev. E **85**, 041924 (2012).

[27] B. R. Parry, I. V. Surovtsev, M. T. Cabeen, C. S. O'Hern, E. R. Dufresne, and C. Jacobs-Wagner, The bacterial cytoplasm has glass-like properties and is fluidized by metabolic activity, Cell **156**, 183 (2014).

[28] S. Stylianidou, N. J. Kuwada, and P. A. Wiggins, Cytoplasmic dynamics reveals two modes of nucleoid-dependent mobility, Biophys. J. **107**, 2684 (2014).

[29] E. R. Weeks, J. C. Crocker, A. C. Levitt, A. Schofield, and D. A. Weitz, Three-dimensional direct imaging of structural relaxation near the colloidal glass transition, Science **287**, 627 (2000).

[30] A. G. Cherstvy, A. V. Chechkin, and R. Metzler, Anomalous diffusion and ergodicity breaking in heterogeneous diffusion processes, New J. Phys. **15**, 083039 (2013).

[31] A. V. Chechkin, F. Seno, R. Metzler, and I. M. Sokolov, Brownian yet Non-Gaussian Diffusion: From Superstatistics to Subordination of Diffusing Diffusivities, Phys. Rev. X **7**, 021002 (2017).

[32] A. Ahmadzadegan, A. Ardekani, and P. Vlachos, "Estimation of the probability density function of random displacements from images", Purdue University Research, doi: 10.4231/34TJ-S109 (2020).

[33] https://github.rcac.purdue.edu/PavlosVlachosGroup/iPED.git.